NANO · MICRO small
www.small-journal.com

Optimal Coatings of Co_3O_4 Anodes for Acidic Water Electrooxidation

Xuan Minh Chau Ta, Thành Trần-Phú, Jodie A. Yuwono, Thi Kim Anh Nguyen, Anh Dinh Bui, Thien N. Truong, Li-chun Chang, Elena Magnano, Rahman Daiyan, Alexandr N. Simonov, and Antonio Tricoli**

Implementation of proton-exchange membrane water electrolyzers for large-scale sustainable hydrogen production requires the replacement of scarce noble-metal anode electrocatalysts with low-cost alternatives. However, such earth-abundant materials often exhibit inadequate stability and/or catalytic activity at low pH, especially at high rates of the anodic oxygen evolution reaction (OER). Here, the authors explore the influence of a dielectric nanoscale-thin oxide layer, namely Al_2O_3, SiO_2, TiO_2, SnO_2, and HfO_2, prepared by atomic layer deposition, on the stability and catalytic activity of low-cost and active but insufficiently stable Co_3O_4 anodes. It is demonstrated that the ALD layers improve both the stability and activity of Co_3O_4 following the order of $HfO_2 > SnO_2 > TiO_2 > Al_2O_3$, SiO_2. An optimal HfO_2 layer thickness of 12 nm enhances the Co_3O_4 anode durability by more than threefold, achieving over 42 h of continuous electrolysis at 10 mA cm^{-2} in 1 M H_2SO_4 electrolyte. Density functional theory is used to investigate the superior performance of HfO_2, revealing a major role of the $HfO_2|Co_3O_4$ interlayer forces in the stabilization mechanism. These insights offer a potential strategy to engineer earth-abundant materials for low-pH OER catalysts with improved performance from earth-abundant materials for efficient hydrogen production.

1. Introduction

Water electrolysis powered by renewable electricity to produce green hydrogen offers a promising route for achieving a carbon-neutral economy.[1–4] To date, there are four most developed water electrolysis technologies, namely alkaline water electrolysis (AWE), anion-exchange membrane water electrolysis (AEMWE), solid oxide electrolysis (SOE), and proton-exchange membrane water electrolysis (PEMWE), each coming with specific benefits and limitations.[5] While AWE and AEMWE can utilize low-cost electrocatalysts to promote water splitting at low to moderate temperatures under alkaline conditions, their overall efficiencies are limited by the low operating current densities.[6,7] SOE is a highly efficient method with low energy consumption and high purity hydrogen production, although operating at high temperatures (up to 1200 °C) and therefore requiring specialized materials and facilities.[5]

X. M. C. Ta, T. Trần-Phú, T. K. A. Nguyen, A. Tricoli
Nanotechnology Research Laboratory
College of Engineering and Computer Science
The Australian National University
Canberra, ACT 2601, Australia
E-mail: thanh.tran@anu.edu.au; antonio.tricoli@anu.edu.au
X. M. C. Ta, T. Trần-Phú, T. K. A. Nguyen, A. Tricoli
Nanotechnology Research Laboratory
Faculty of Engineering
University of Sydney
Sydney, NSW 2006, Australia
J. A. Yuwono
School of Chemical Engineering & Advanced Materials
The University of Adelaide
Adelaide, SA 5005, Australia
The ORCID identification number(s) for the author(s) of this article can be found under https://doi.org/10.1002/smll.202304650

DOI: 10.1002/smll.202304650

J. A. Yuwono
College of Engineering and Computer Science
Australian National University
Canberra, ACT 2601, Australia
A. D. Bui, T. N. Truong, L.-chun Chang
School of Engineering
The Australian National University
Canberra, ACT 2601, Australia
E. Magnano
IOM-CNR
Istituto Officina dei Materiali
AREA Science Park Basovizza
Trieste 34149, Italy
R. Daiyan
Particles and Catalysis Research Laboratory
School of Chemical Engineering
The University of New South Wales
Sydney, NSW 2052, Australia
A. N. Simonov
School of Chemistry
Monash University
Clayton, VIC 3800, Australia

Alternatively, PEMWE presents benefits of operation under mild temperature conditions using compact design cells with very high output current densities up to 10 A cm^{-2} and high energy efficiencies.[8–11]

Nonetheless, a key limitation of the PEMWE technology is the reliance on anode catalysts based on iridium, which prevents its large-scale implementation due to the scarcity of this noble metal.[12] To address this challenge, noble-metal-free electrocatalysts for the oxygen evolution reaction (OER) need to be developed. However, achieving both high stability and activity for the OER at low pH is problematic even for the most robust iridium-oxide-based catalysts.[13–19] Instability is even more of an issue for non-noble-metal-based catalysts.[20–24] For example, cobalt oxide (Co_3O_4) is relatively active towards the acidic OER , but its application is hindered by its low stability at low pH.[25,26]

One promising approach to improve the longevity of low-pH OER catalysts is to couple active elements with more thermodynamically stable or self-healing oxide matrixes, including PbO_2, TiO_2, BiO_x, SbO_x, and, to some extent, MnO_x.[22,23,27–31] Arguably, this catalyst design strategy has provided some of the best results in terms of balancing stability and activity. Recognizing that corrosion of non-noble metals during the operation of an OER catalyst is often unavoidable, the stability of some materials can be significantly improved through the intentional introduction of the metal precursors into the electrolyzed solutions, enabling operation at very high current densities and temperatures up to 80 °C.[31–35] However, operation of such systems in a practical electrolyzer device is yet to be demonstrated. Potential practical challenges include the poisoning of the proton-exchange membrane and the cathodes.

Another strategy to protect OER anodes against corrosion, while maintaining high catalytic activity, is to coat the electrocatalyst layer with a more stable passivation layer. Maintaining a nm-thickness of this layer allows for sufficiently high mass- and charge-transfer rates to sustain the electrocatalytic reactions, while significantly suppressing the dissolution of the catalyst.[36–39] Among thin-film deposition methods, atomic layer deposition (ALD) enables the formation of high-quality conformal layers with accurately controlled thickness.[36–39] A reasonably broad range of materials has been examined as protection layers for the OER catalysts with promising results demonstrated.[40–45] However, studies under acidic conditions are limited to TiO_2,[39–42] SiO_2,[46] or Al_2O_3[43] coatings on Co_3O_4, IrO_x, RuO_2, or WO_3 electrocatalysts, respectively. Besides, few studies have compared the chemical stability and corrosion resistance of some ultrathin oxide layers (Al_2O_3, TiO_2, ZnO, HfO_2, and ZrO_2) as protection layer in different electrolyte conditions, but they have not been comprehensively investigated in acidic anodic conditions.[44,45,47]

The present study aims to improve our understanding of the required properties for the passivation layer to improve the stability and electrochemical activity of earth-abundant OER catalysts for acidic electrolysis. To this end, we investigated the electrocatalytic activity of Co_3O_4 anodes modified with nanometer-thin conformal protective TiO_2, Al_2O_3, SnO_2, SiO_2, and HfO_2 layers, fabricated by ALD, for water electrooxidation in an H_2SO_4 electrolyte at pH 0. Through a combination of electrochemical, microscopic, spectroscopic, and theoretical studies, we reveal insights into the interrelation between the chemical nature and thickness of the coatings, electrocatalytic activity, and stability of the modified anodes.

2. Results and Discussion

2.1. Physical Characterization

The water-oxidizing anodes examined herein were prepared by deposition of cobalt layers on fluorine-doped tin oxide (FTO) glass substrates by sputtering followed by the annealing process. This resulted in the formation of a dense uniform layer of Co_3O_4 particles, confirmed by scanning electron microscopy (SEM), X-ray diffraction (XRD), and Raman spectroscopy (**Figure 1**a and Figure S1, Supporting Information). The uniformity of the Co_3O_4 layer, having a thickness of ≈360 nm, was confirmed by cross-sectional SEM images (Figure 1b) and energy-dispersive X-ray spectroscopic mapping (EDS) (Figure 1c–f). Such planar Co_3O_4 anodes were coated by a thin Al_2O_3, SiO_2, TiO_2, SnO_2, or HfO_2 passivation layer by ALD, which were indiscernible in the SEM images and undetectable by XRD and Raman (Figures S1–S3, Supporting Information). However, the corresponding EDS data confirms the presence and uniform distribution of the coating elements over the Co_3O_4 films (Figure S3, Supporting Information). For the initial screening studies, the thickness of the ALD layer was kept similar within 3–4 nm, as measured by ellipsometry (**Table 1**).

To probe the chemical state of the elements in the produced electrodes, X-ray photoelectron spectroscopic (XPS) analysis was undertaken (Figure S4, Supporting Information, and **Figure 2**). The Co 2p spectrum of the unmodified Co_3O_4/FTO electrode is consistent with the published data for the cobalt(II, III) oxide (Figure 2a).[39,48–50] After deposition of the coating layer, the features of the Co 2p spectra remained unaltered although the intensity of the peaks was slightly reduced (Figure S4, Supporting Information). Secondary elements forming the nanometer-thick overlayers were clearly detectable by XPS, with the peak positions corresponding to Al_2O_3 (74.4 eV; Figure 2b),[51,52] SiO_2 (Si^{4+} 103.5 and Si^{3+} 101.8 eV; Figure 2c),[53] TiO_2 (Ti^{4+} $2p_{3/2}$ 459 and Ti^{4+} $2p_{1/2}$ 465 eV; Figure 2d),[39,51,54,55] SnO_2 (Sn^{4+} $3d_{5/2}$ 486.8 and Sn^{4+} $3d_{3/2}$ 495.2 eV; Figure 2e),[51] and HfO_2 (Hf^{4+} $4f_{7/2}$ 17.5 and Hf^{4+} $4f_{5/2}$ 19.2 eV; Figure 2f).[51,56] Together, these physical characterization results indicate the successful deposition of nanoscale oxide coatings on the Co_3O_4/FTO surface and no detectable changes to the properties of the underlying Co_3O_4 layers induced by the ALD.

The electrochemically active surface area (ECSA) of the catalytic surface was derived from the capacitance values measured by cyclic voltammetry in the potential range devoid of significant faradaic processes (Figure S5, Supporting Information).[57,58] Deposition of the overlayers onto sputtered Co_3O_4/FTO electrodes did not change the ESCA values significantly, which resulted in relatively similar double layer capacitance values (Figure S5h, Supporting Information), estimated from the slopes of the capacitive currents as a function of scan rates between bare and coated Co_3O_4 surfaces.[59–61] To estimate the ECSA values, a specific capacitance of a smooth surface such as a polished glassy carbon under identical pH and applied potential conditions might be used as an approximate reference;[61,62] however, one should recognize obvious differences in the chemical nature and

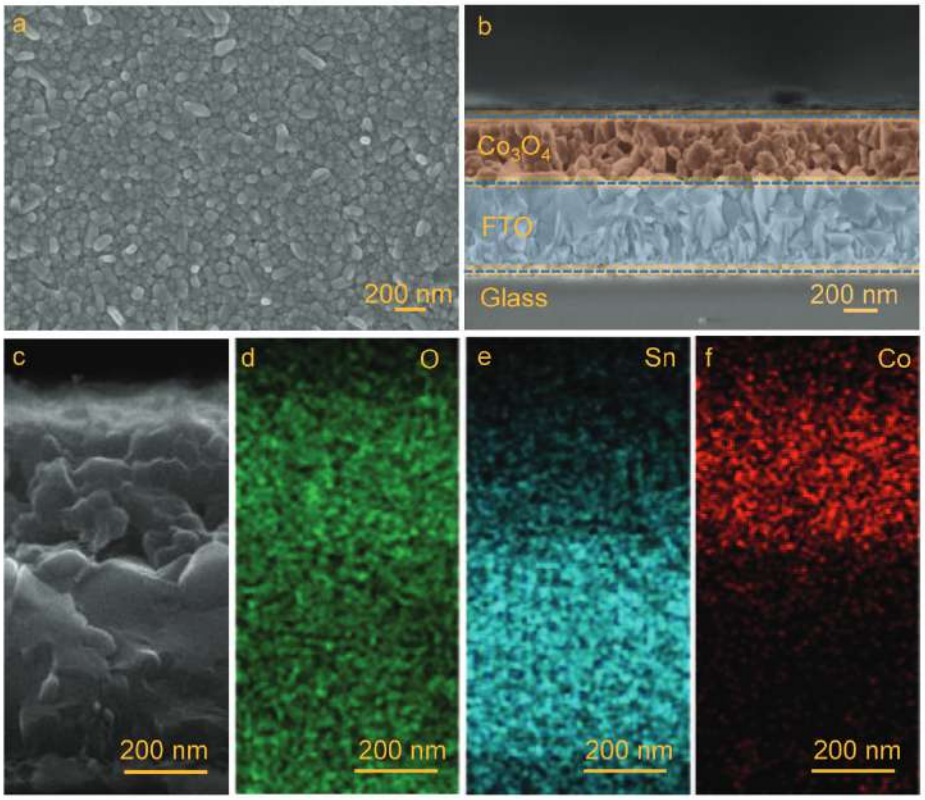

Figure 1. Microscopic characterization of a Co_3O_4/FTO electrode. a) Top and b) cross-sectional SEM images. Micrograph in panel (b) was colored post-analysis to assist the visualization of Co_3O_4 (orange), FTO (blue), and glass (grey); dashed lines highlight the boundaries between different layers. c) Higher magnification SEM and d–f) corresponding EDS elemental mapping of d) oxygen (green), e) tin (turquoise), and f) cobalt (red) for the Co_3O_4/FTO electrode.

double-layer structure between the metal oxides and carbon electrodes. In our study, a specific capacitance of 0.042 mF cm^{-2} at 0.81 V versus a reversible hydrogen electrode (RHE) was measured in 1 M H_2SO_4 for a polished glassy carbon surface. The approximate ECSA values of pristine and ALD-coated Co_3O_4 anodes were then obtained (Table 1).

2.2. Electrocatalytic Performance

The OER electrocatalytic activity of the bare and coated Co_3O_4 anodes was studied in 1 M H_2SO_4 electrolyte with pH 0 at ambient temperature. First, the Co_3O_4 films were investigated using electrochemical impedance spectroscopy (EIS) at 0.3 V (Figure S6, Supporting Information) and 1.8 V versus RHE (Figure S7, Supporting Information). The series resistance (R_s) and charge transfer resistance of the Co_3O_4/FTO with and without the protective oxide layers (R_{ct}) were determined by fitting a simplified circuit model (inset circuit in Figures S6 and S7, Supporting Information),[63-65] with the fitted values presented in Tables S1 and S2, Supporting Information. The results show that the electrical conductivity decreases upon deposition introduction of the dielectric coating, following the order of bare Co_3O_4 > HfO_2/Co_3O_4 > SnO_2/Co_3O_4 > TiO_2/Co_3O_4 > Al_2O_3/Co_3O_4 >

Table 1. Summary of the key properties of the investigated Co_3O_4/FTO electrodes.

Overlayer	ECSA [$cm^2\ cm_{geom.}^{-2}$]	Overlayer thickness [nm]	$E_{10\ mA\ cm}^{-2}$ [V versus RHE]	Stability at 10 mA cm^{-2} [h][a)]
none	3.43	0	1.96	12
Al_2O_3	3.30	3.1	2.06	20
SiO_2	3.08	3.9	2.06	23
TiO_2	3.30	3.1	2.02	27
SnO_2	3.26	3.9	2.01	28
HfO_2	3.43	3.0	1.93	32

$E_{10\ mA\ cm}^{-2}$: initial quasi-stabilized potential required to sustain the OER rate of 10 mA cm^{-2} derived from 30 min chronopotenitometric measurements; [a)] Stability at 10 mA cm^{-2}: point of time when potential starts to abruptly increase during extended OER tests at 10 mA cm^{-2}.

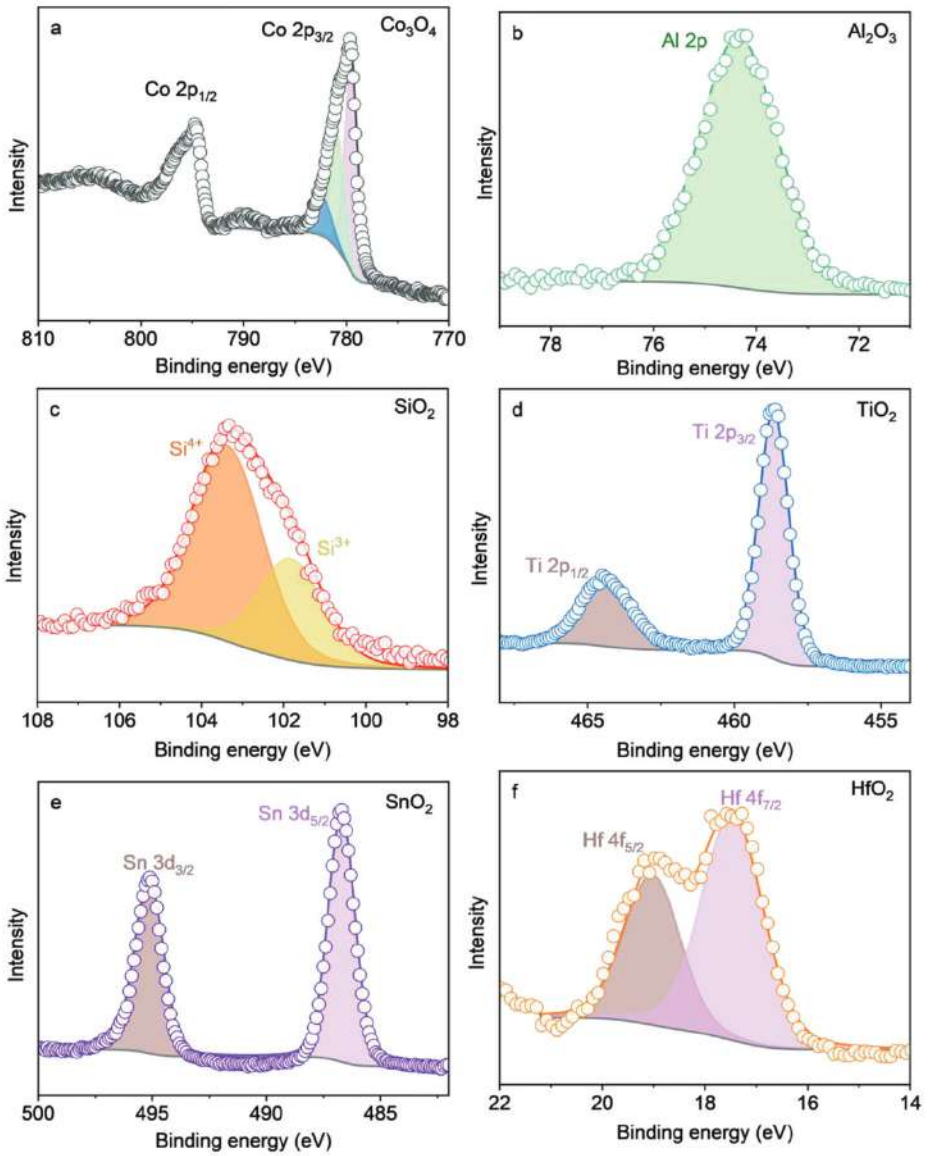

Figure 2. High-resolution XP spectra of a) Co 2p, b) Al 2p, c) Si 2p, d) Ti 2p, e) Sn 3d, and f) Hf 4f (colored dots) and corresponding fitting (solid lines – cumulative curve; filled areas – individual peak components; grey line – background) for a) unmodified Co_3O_4/FTO, and Co_3O_4/FTO electrodes coated 3–4 nm thick overlayers of b) Al_2O_3, c) SiO_2, d) TiO_2, e) SnO_2, and f) HfO_2.

SiO_2/Co_3O_4, indicating a reduction in the charge transfer kinetics of coated electrodes compared to the bare anodes, despite their small thickness of 3 to 4 nm.(Figures S6 and S7 and Tables S1 and S2, Supporting Information).[63–65]

The water oxidation performance in 1 M H_2SO_4 of the Co_3O_4/FTO anodes with and without protective layers was further compared using voltammetric and chronopotentiometric data (**Figure 3a–c**). Linear sweep voltammetry (LSV) curves of unmodified samples showed an oxidation peak at ≈1.65 V versus RHE, which was attributed to the oxidation of the lattice Co species in Co_3O_4 to a higher oxidation state during the anodic polarization. This oxidation peak could be observed more clearly when the scan rate was increased to 20 and 50 mV s^{-1} (Figure S8, Supporting Information).[39,66,67] Amongst the coating layers, only HfO_2 produced a slight increase in the electrocatalytic activity at potentials more positive than ≈1.8 V versus RHE as compared to unmodified Co_3O_4/FTO (Figure 3d and Table 1). All other oxide coatings (Al_2O_3, TiO_2, SnO_2, SiO_2) decreased electrocatalytic current but did not completely suppress it, indicating that the charge/mass transport through these very thin layers is sufficient to sustain the OER. These trends were confirmed by chronopotentiometric measurements at 10 mA cm^{-2}, showing that the HfO_2/Co_3O_4/FTO requires a potential of ≈1.93 V to sustain this OER rate, which is ≈0.03 V better than the bare Co_3O_4/FTO. All other coatings required a 0.05–0.1 V more positive potentials required to achieve 10 mA cm^{-2} (Figure 3d and

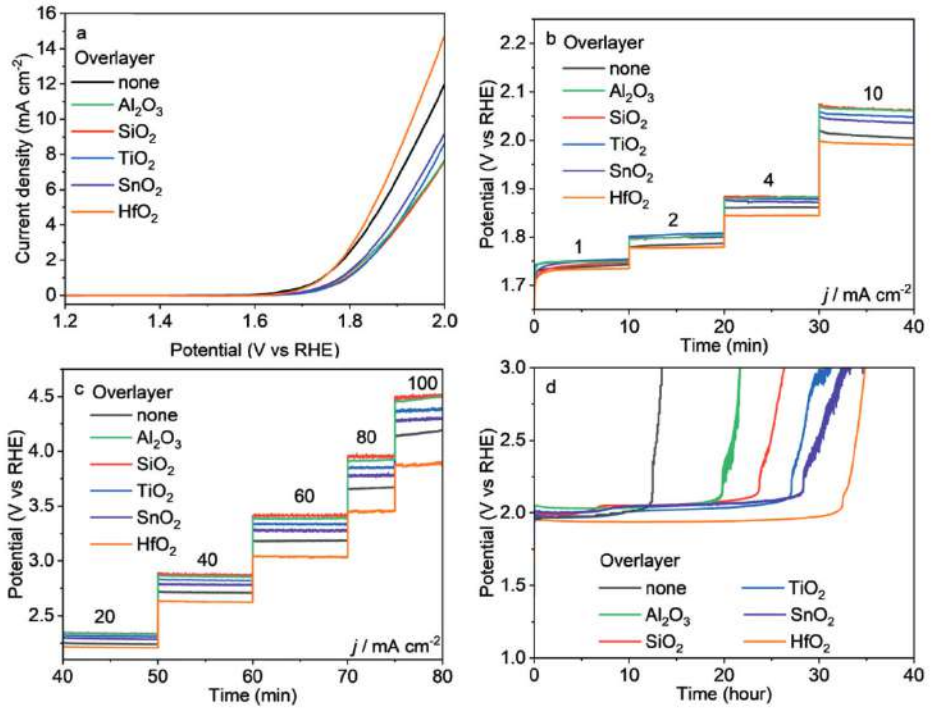

Figure 3. Electrochemical characterization of the Co_3O_4/FTO electrodes without (black) and with a 3–4 nm thick overlayer of Al_2O_3 (green), SiO_2 (green), TiO_2 (blue), SnO_2 (purple), and HfO_2 (orange). a) Quasi-stabilized voltammetric sweeps (third scan, scan rate 0.005 V s^{-1}), b,c) chronopotentiograms at varied current densities b) 1 to 10 mA cm^{-2} and c) 20 to 100 mA cm^{-2}, and d) chronopotentiometric curves recorded at 10 mA cm^{-2} in 1 M H_2SO_4. Currents are normalized to the geometric surface area.

Table 1). Additionally, the apparent Tafel slopes of these anodes were analyzed. Figure S9, Supporting Information, shows the slopes of the semilogarythmic dependencies of potential on current density are similar , suggesting similar reaction kinetics with and without coating layers.

Importantly, a significant enhancement in the electrode stability was observed for all nanoscale coatings. The bare Co_3O_4 maintained a stable potential of ≈1.96 V versus RHE for a current of 10 mA cm^{-2} for less than 12 h before displaying a sharp increase in the potential, which indicates the loss of the catalytically active Co_3O_4 layer. The latter was confirmed by the inductively coupled plasma mass spectroscopy (ICP-MS) analysis (Figures S18 and S20, Supporting Information). The Al_2O_3 and SiO_2 layers prolonged the durability of the electrodes under the examined conditions to 20 and 23 h, respectively, while the TiO_2 and SnO_2 layers improved the stability to ≈27–28 h. Notably, the HfO_2 layer not only improved the electrocatalytic activity of the Co_3O_4 electrode but also enhanced its stability to 32 h, the best protective layer amongst the oxides examined herein.

To map the anode morphological changes during the OER, we carried out SEM analysis of the samples tested at 10 mA cm^{-2} for 8 and 24 h (**Figures 4** and **5**). Top-view images reveal pitting of the anode surface, with the size and density depending on the composition of the coating and the duration of the tests. For the unmodified Co_3O_4, large holes of hundreds of nm in size were already observed after 8 h and essentially no catalyst was detectable after 24 h (Figure 4a). This was corroborated by the side-view imaging and SEM-EDS elemental mapping, showing a significant reduction in the Co_3O_4 layer thickness from 360 to 200 nm after 8 h and its almost complete disappearance after 24 h (Figure 5a). These results are consistent with the SEM-EDS mapping presented in Figure S10, Supporting Information, which revealed the disappearance of the Co element in unmodified samples after 24 h.

When coated with nanosized passivation layers, holes of varying sizes appeared on the surface for all electrodes after 8 h except those coated with HfO_2 (Figure 4b–f). The Al_2O_3/Co_3O_4 and SiO_2/Co_3O_4 anodes showed a similar morphology with hole diameters ranging from 200 to 400 nm after 8 h (Figure 4b,c), while fewer and smaller holes were observed on the TiO_2/Co_3O_4 (Figure 4d) and SnO_2/Co_3O_4 anodes (Figure 4e). At the same time, the density of these pitting sites was low for the coated anodes, and no significant changes in the thickness of the underlying Co_3O_4 anode were detected after 8 h for all overlayers examined (Figure 5b–f). Increasing the electrolysis time to 24 h, resulted in a complete loss of the Co_3O_4 layer for the anodes coated with Al_2O_3 and SiO_2 (Figures 4b,c and 5b,c). These observations are consistent with the results of the galvanostatic tests showing a sharp increase in the applied potential before 24 h (Figure 3d) and SEM-EDS mapping (Figures S11 and S12, Supporting Information). The TiO_2, SnO_2, and HfO_2 coatings were able to preserve the Co_3O_4 anode for up to 24 h (Figure 4d–f) with the residual Co_3O_4 thickness following the order of HfO_2/Co_3O_4 > SnO_2/Co_3O_4 > TiO_2/Co_3O_4 (Figure 5d–f), consistently with the galvanostatic measurements (Figure 3d and Table 1) and SEM-EDS mapping (Figures S13–S15, Supporting Information).

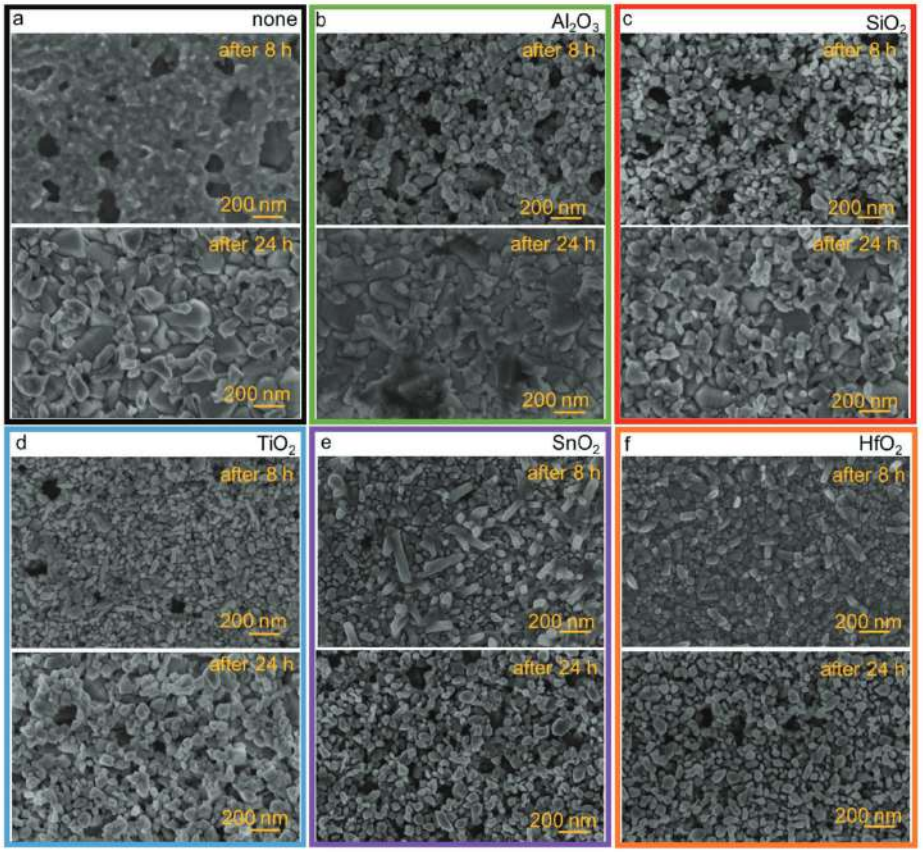

Figure 4. Top-view SEM images of a) unmodified Co_3O_4/FTO and Co_3O_4/FTO electrodes coated with 3–4 nm thick coating layers of b) Al_2O_3, c) SiO_2, d) TiO_2, e) SnO_2, and f) HfO_2 after 8 and 24 h of galvanostatic OER tests in 1 M H_2SO_4 at 10 mA cm^{-2}.

As the most stable electrode, changes in the morphology of the HfO_2/Co_3O_4 anode were further investigated by TEM and EDS before and after 24 h tests. TEM images of the as-deposited sample (Figure S16, Supporting Information) revealed agglomerates of thick, crystalline Co_3O_4, covered with an amorphous HfO_2 layer, which was further evidenced by EDS elemental mapping. After 24 h of electrolysis, although we still observe the (220) lattice planes of crystalline Co_3O_4 (Figure S17b–d, Supporting Information), their grains become thinner with the appearance of new holes (Figure S17a,d, Supporting Information) with disappearance of HfO_2 coating layer (Figure S17b,e,f, Supporting Information).

Additionally, electrolytes derived from testing of the Co_3O_4 anodes without and with overcoating layers after 8, 24, and 32 h electrolysis were analyzed with ICP-MS (Table S3 and Figures S18 and S20, Supporting Information). The corrosion rate after 8 h of the OER was the highest (0.49 μmol h^{-1}) for the unmodified electrodes, followed by the Al_2O_3 (0.43 μmol h^{-1}), SiO_2 (0.42 μmol h^{-1}) > TiO_2 (0.38 μmol h^{-1}) > SnO_2 (0.31 μmol h^{-1}) > HfO_2 (0.19 μmol h^{-1}) coated anodes (Table S3 and Figure S18a, Supporting Information). After 24 h electrolysis, the OER activity of the unmodified and Al_2O_3 coated anodes mostly come from the F-doped SnO_2 substrate (Figure S19a, Supporting Information), leading to an applied potential of over 3.2 V versus RHE to maintain a current density of 10 mA cm^{-2} (Figure S19b, Supporting Information). However, the required potential in SiO_2-coated anode was still under 3.2 V versus RHE, indicating the existence of some Co_3O_4 catalyst on the FTO substrate to contribute to the OER activity. For this reason, the amount of dissolved Co in the electrolyte from the SiO_2-coated anode was slightly lower than those in the unmodified and Al_2O_3-coated anodes (Figure S18b, Supporting Information). For TiO_2, SnO_2, and HfO_2 coated anodes, the corrosion rates of Co_3O_4 significantly increased during 24 h of electrolysis, consistent with more pin-holes appearing on the surface of the electrode after 8 h (Figure 4), and less catalyst materials remained on the substrate after 24 h (Figure 5). After 32 h, the amount of etched Co from TiO_2/Co_3O_4/FTO and SnO_2/Co_3O_4/FTO anodes was similar to that from the unmodified samples after 24 h (Figure S18c, Supporting Information), indicating complete dissolution of Co_3O_4. For the HfO_2/Co_3O_4/FTO anode, the dissolution rate of Co_3O_4 detected within 24–32 h was lower compared to those from other electrodes, indicating the efficient protection effect of the HfO_2 layer on the Co_3O_4 electrodes. Additionally, the dissolution of the overlayers from Al, Ti, and Hf was investigated by ICP-MS analysis (Figure S20, Supporting Information). It revealed the dissolved amount of the overcoating layer significantly increased over time. Noticeably, after 24 h, the changes in the amount of

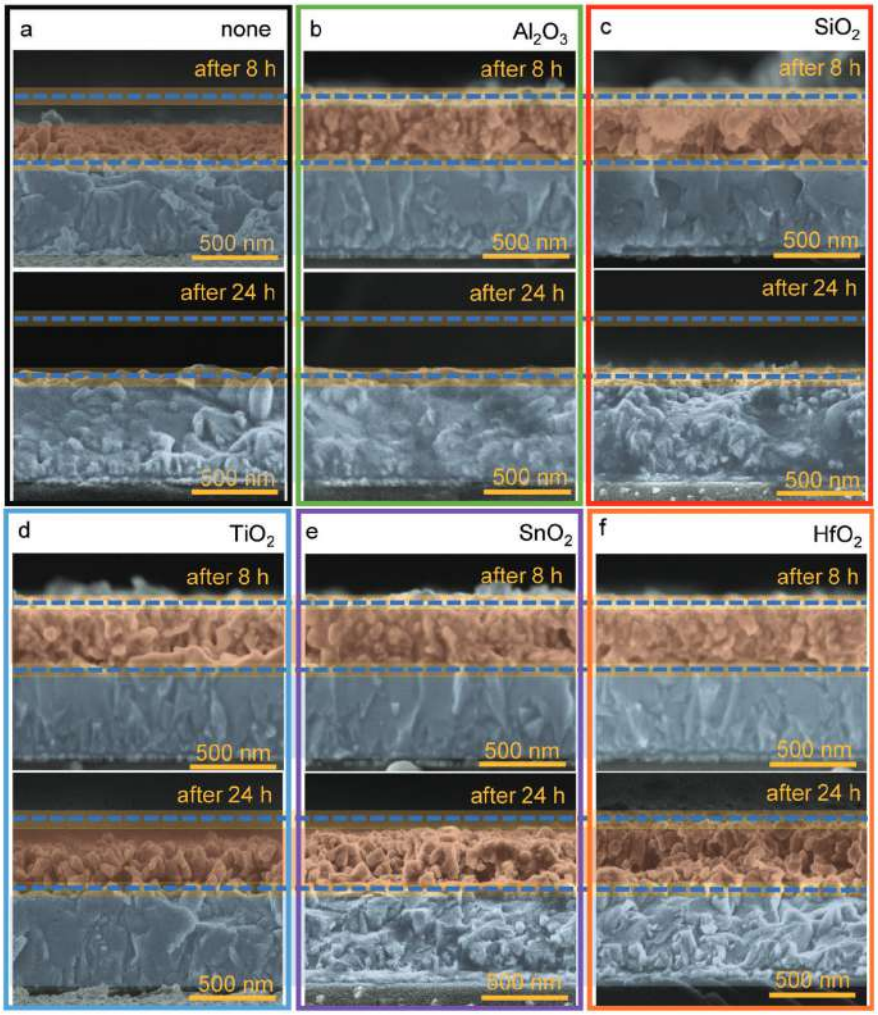

Figure 5. Cross-sectional SEM images of a) unmodified Co_3O_4/FTO and Co_3O_4/FTO anodes coated with 3–4 nm thick overlayers of b) Al_2O_3, c) SiO_2, d) TiO_2, e) SnO_2, and f) HfO_2 after 8 (top) and 24 h (bottom) of galvanostatic OER tests in 1 M H_2SO_4 at 10 mA cm^{-2} (orange: Co_3O_4 electrocatalyst, blue: FTO, and the blue dashed line: the boundary of pristine Co_3O_4 layer).

TiO_2 and HfO_2 were negligible, indicating the nearly complete dissolution of the overlayers.

Collectively, our findings suggest that HfO_2 is the best passivation layer among the investigated dielectric materials. To determine the optimal thickness of HfO_2, we varied its thickness from 3 to 20 nm. Voltammetric and chronopotentiometric analysis of these electrodes indicate that increasing the HfO_2 thickness up to 12 nm does not significantly affect the OER activity of the electrode (**Figure 6**). The results suggest that the mass and charge transport in anodes coated with less than 12 nm HfO_2 thickness was still sufficient to catalyze the reaction. However, deposition of a 20 nm layer substantially deteriorated the OER performance, increasing the potential to ≈2.2 V versus RHE, ≈0.27 V higher than that of the unmodified Co_3O_4/FTO, to achieve an OER rate of 10 mA cm^{-2}. It is attributed to a strong decrease in the conductivity of the anodes, which is reflected by an increase of charge transfer resistance from 13.5 to 293.6 kΩ with increasing HfO_2 thickness from 0 to 20 nm in the EIS measurements (Figure S21 and Table S4, Supporting Information). Extended durability tests indicate that coating of Co_3O_4 with a 12 nm thick HfO_2 can prolong the stability of the OER performance to 42 h (Figure 6b). This is 10 h more than that with the 3 nm HfO_2 coating and a 3.5-time increase over that of the unmodified electrode. This is also a considerably good stability in comparison to acidic water oxidation at low pH (Table S5, Supporting Information). Notably, further increasing the thickness to 20 nm did not improve the stability. This might be attributed to the more positive potential applied to the electrode during the test due to the lower electrocatalytic activity (Figure 6b). Likewise, the impact of the coating thicknesse (3, 6, 8, and 10 nm) of Al_2O_3 and TiO_2 on the catalytic activity and stability of the anodes was also investigated. The chronopotentiometric results (Figure S22, Supporting Information) indicate that the optimal Al_2O_3 and TiO_2 thicknesses are in the range of 3–6 nm. Thinner or thicker coating layers decrease the stability and activity of the electrodes as similarly observed from the HfO_2 coating and reported in the literature.[39,68]

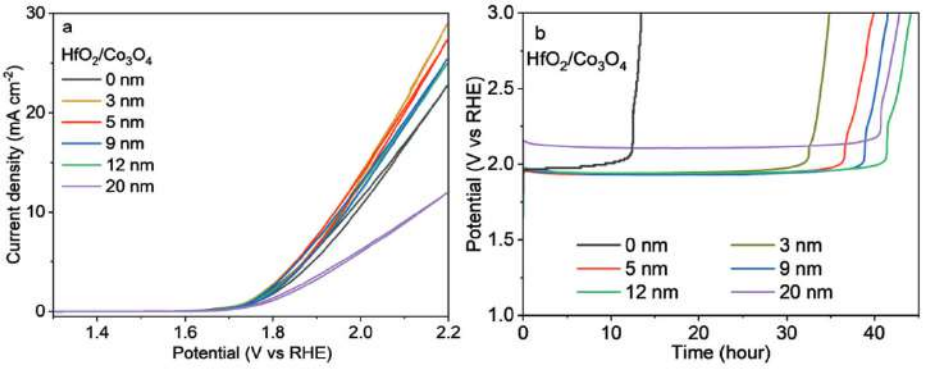

Figure 6. Electrochemical characterization of the Co_3O_4/FTO electrodes coated with different HfO_2 thicknesses. a) Quasi-stabilized cyclic voltammetric sweeps (third scan with scan rate 0.005 V s^{-1}), and b) chronopotentiometric curves recorded at 10 mA cm^{-2} in 1 M H_2SO_4. Currents are normalized to the geometric surface area.

Importantly, their activity could not be retained after 27 h OER, which is by far shorter than 42 h obtained from the anode coated with an optimized HfO_2 layer.

The 12 nm thick HfO_2 coating had the best stability and activity and thus was further investigated with an extended durability test in0.1 M H_2SO_4 solution with pH ≈ 1 (Figure S23, Supporting Information). This anode required ≈2.05 V versus RHE to achieve an oxygen evolution rate of 10 mA cm^{-2} and remained stable for a duration of ≈70 h. However, the applied potential surged after 70 h of continuous electrolysis, which could be attributed to the significant loss of the active electrocatalysts, leaving the inactive FTO surface (Figure S24, Supporting Information). Though the (12 nm) HfO_2 layer can prolong the stability and maintain the OER activity of the electrode for nearly 70 h, the anode still dissolved under anodic OER in strong acid, which indeed can dissolve noble metal oxides, such as RuO_x or IrO_x, to a certain extent.[16,69,70] The OER performance and stability of the HfO_2/Co_3O_4/FTO anodes are compared with recent stable acidic OER catalysts in Table S5, Supporting Information. Many of these anodes achieved a prolonged lifetime due to a higher mass loading or a thicker catalyst layer.[39,71–74] To compare the stability of different catalysts reported in various publications, the catalyst lifetime was normalized to its mass and thickness. The normalized stabilities of our HfO_2 coated anode are 262.5 h mg_{co}^{-1} and 113 h μm^{-1} at a pH of 0, and 500 h mg_{co}^{-1} and 215 h μm^{-1} at a pH of 1, respectively, for a current of 10 mA cm^{-2}. These outperform most of the recently reported acidic OER anodes made of earth-abundant materials (Table S5, Supporting Information).[39,71–74] Exclusively, the superior durability of Co_2MnO_4 and $Ni_{0.5}Mn_{0.5}Sb_{1.7}O_y$, achieving 208 h mg_{co}^{-1} for a current of 100 mA cm^{-2} and 1292.3 h mg^{-1} for a current of 10 mA cm^{-2}, respectively, can be attributed to the stability of the Mn and/or Sb matrix.[75,76] However, they require a more complex preparation process and a precise composition. The implementation of a surface protective layer shown in this study provides a promising direction for a wide range of catalyst materials for acidic OER.

To understand the production efficiency, the Faradaic efficiency (FE) of O_2 evolved from HfO_2/Co_3O_4/FTO and Co_3O_4/FTO anodes were measured (Figure S25, Supporting Information). Both samples reached stable FE efficiency at nearly 100%, confirming the ALD coating layers have negligible impacts on the OER selectivity of the Co_3O_4 electrocatalyst.

Our electrochemical and spectroscopic characterization showed that ALD coating results in a slight difference in OER activity but a significant enhancement of the stability, following the order of HfO_2 > SnO_2 > TiO_2 > SiO_2, Al_2O_3. Since the difference in the thickness of the coating layers was minimal, the changes in the stability can be attributed to the intrinsic material properties of the overlayers during the OER in an acidic environment. Such intrinsic properties can be determined by the thermodynamic stability in connection with the underlying Co_3O_4 catalysts, which are further supplemented in the theoretical calculations below.

2.3. Theoretical Calculations

Our experimental results show that the stability of the coated anodes follows the order of HfO_2 > SnO_2 > TiO_2 > Al_2O_3, SiO_2. However, when deriving the thermodynamic stability of the oxide coatings from Pourbaix diagrams, SnO_2, SiO_2, and TiO_2 are expected to be more stable at low pH conditions (Figure S26, Supporting Information).[77] We hypothesize that in addition to the thermodynamic stability of the coating, the bonding strength between the Co_3O_4 surface and the overlayer also plays an important role. To further investigate and gain insights into such bonding strength, we carried out density functional theory (DFT) calculations (**Figure 7**).

By employing simplified models where the (110) surface of Co_3O_4 is bonded with the coating molecule via an oxygen atom,

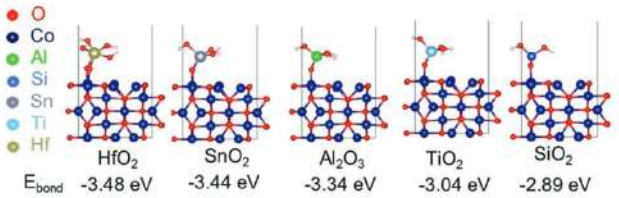

Figure 7. Theoretical calculations of the bonding energy (E_{bond}) between (110) facet of Co_3O_4 and the coating oxides using simplified models: from left to right, Co_3O_4-HfO_2, -SnO_2, -Al_2O_3, -TiO_2, and -SiO_2.

our finding reveals that the Co—O—Hf bonding energy (−3.48 eV) is the strongest, followed by Co—O—Sn (−3.44 eV), Co—O—Al (−3.34 eV), Co—O—Ti (−3.04 eV), and Co—O—Si (−2.89 eV). The (110) facet was used in the modeling as it is one of the specific lattices of the Co_3O_4 spinel reflected in XRD patterns and high-resolution TEM analysis. It is worth noting that although the Co—O—Al bonding energy is stronger than those of Ti and Si, Al_2O_3 is less thermodynamically stable according to the data shown in the Pourbaix diagram at low pH compared to TiO_2 and SiO_2 (Figure S26, Supporting Information). This indicates that both the thermodynamic stability of coating oxides and bonding strength between the underlying and coating layers should be considered when assessing the durability of oxygen evolution catalysts at low pH. This implies the effectiveness of combining theoretical and experimental studies, providing directions for acidic water electrolysis studies, including self-healing strategy.[29,31,33,34]

3. Conclusions

In this study, we presented a systematical investigation of the key properties of nanoscale dielectric layers to stabilize earth-abundant Co_3O_4 OER anode electrocatalysts in highly acidic conditions. Dielectric layers of Al_2O_3, SiO_2, TiO_2, SnO_2, and HfO_2 were conformally deposited on Co_3O_4 anodes by ALD. We reveal that though the nanoscale coatings cannot prevent the ultimate dissolution of the underlying Co_3O_4, they can significantly improve the anode longterm stability, while maintaining the Co_3O_4 catalytic activity with the order of $HfO_2 > SnO_2 > TiO_2 > Al_2O_3$, SiO_2. Our theoretical calculations suggest that this may be attributed to the stronger bonding energy of the $Co_3O_4|HfO_2$ interface as compared to other oxide coatings, highlighting the importance of the interfacial engineering between the coating and coated layers. The optimally coated anode with a HfO_2 thickness of 12 nm was able to retain a current density of 10 mA cm^{-2} at ≈1.95 V versus RHE for > 42 h in an H_2SO_4 electrolyte pH 0. These insights provide guidelines for engineering coatings of non-platinum group metal (non-PGM) anode catalysts for the acidic electrolysis. While this study was conducted in conventional H-cell tests at pH 0, experiments in a PEMWE, where local pH, current densities, and temperature are higher, should be demonstrated to assess the activity and stability of the anode catalysts under practical conditions.

4. Experimental Section

Materials: All the chemical reagents and solvents for the material synthesis were used as received without any further purification. Ultrapure deionized water (resistivity 18.2 MΩ cm^{-1}) was used in preparing aqueous solutions in all experiments.

Substrate Preparation: The fluorine-doped tin oxide (FTO) glass substrate 10 × 35 mm was purchased from OPV Tech. The substrate was first cleaned with ethanol and water and dried. The exposed geometric area of the substrate to the electrolyte solutions was 1 cm^2.

Fabrication of Co_3O_4 Catalysts: Cobalt (Co) film was deposited onto the FTO glass substrate by DC magnetron sputtering in 1200 s at an applied bias of 600 W. Then, they were annealed at 550 °C for 2 h with a ramp rate of 2 °C min^{-1} to obtain the cobalt oxide (Co_3O_4) layer. The mass loading of the Co_3O_4 anode was estimated with the mass density extracted from The Materials Project for cubic Co_3O_4 materials (6.1 g cm^{-3}).[77]

Conformal TiO_2, Al_2O_3, SiO_2, SnO_2, and HfO_2 films were deposited onto the $Co_3O_4|FTO$ anodes using a plasma-assisted atomic layer deposition (PA-ALD) system (PicoSun-Sunale) with argon and oxygen plasma as the co-reactants. Al, Si, Ti, Sn, and Hf sources were trimethylaluminum ($AlCl_3$), silane (SiH_4), titanium tetrachloride ($TiCl_4$), tetrakis (dimethylamino) tin ($[(CH_3)_2N]_4Sn$), tetrakis (ethylmethylamido) hafnium ($[(CH_3)(C_2H_5)N]_4Hf$), respectively. SiO_2 and SnO_2 were deposited by the PA-ALD system at 300 and 83 °C, respectively. The vessels of three hot sources, including SiO_2, SnO_2, and HfO_2, were heated at 45, 55, and 120 °C throughout the ALD deposition process. HfO_2, Al_2O_3, and TiO_2 were deposited at ambient temperature and the vessels of TiO_2 and Al_2O_3 source were kept at room temperature. The thickness of the ALD coating layer was precisely controlled by tuning the ALD deposition cycles.

Material Characterization: The morphology of the films was investigated using a field-emission scanning electron microscope (FESEM) Zeiss Ultra Plus operating at 3 kV without coating. Samples for SEM were prepared by fixing the cut pieces of the electrode on the specimen stubs using carbon tape.

XRD patterns were recorded by a D2 Phaser Bruker system with Cu Kα radiation of average wavelength 1.54056 Å at a scan rate of 1.17 deg min^{-1}. The XRD results were obtained by direct measurement of the samples on FTO substrates. Raman spectra were recorded at room temperature by LabRAM HR (Horiba) evolution CCD camera 532 delta diode laser, using grating 1800 (500 nm). The laser power was 22 mW with 100 percent intensity. The spectra were collected at 50 s of acquisition time.

XPS analysis was performed using a calibrated ESCALAB250Xi spectrometer (Thermo Scientific, UK) with a monochromated Al Kα source at a power of 120 W (13.8 kV × 8.7 mA). The base pressure in the main vacuum chamber during analysis was typically between 10^{-9} and 10^{-8} mbar. Survey spectra were acquired at a pass energy of 160 eV. To obtain more detailed information about the chemical structure, oxidation states, and so forth, high-resolution spectra were recorded at 20 eV pass energy (yielding a typical peak width for polymers of ≈1 eV). Spectra were collected at normal emission. The data was analyzed using CasaXPS software version 2.3.25 PR1.0. Adventitious C 1s (284.8 eV) peak was used to calibrate the spectra.

The coating thicknesses were measured using a JA Woollam M2000D ellipsometer. The measurements were conducted with the thin oxide layers on the double-side polished Si wafer.

The ICP-MS was performed by Nexion5000 from PerkinElmer, USA. Samples for ICP-MS measurements were prepared by using 3 mL electrolyte in the continuous flow. The amount of Co etched in the electrolyte was detected by Co-59 mass, Helium KED mode, internal standard-Rh-103.

Electrochemical Characterization: All electrochemical measurements in this study were carried out with a BioLogic electrochemical workstation using a customized two-compartment separated by a Nafion@117 membrane (sourced from FuelCellStore). In the electrochemical tests, the ALD coating layer/Co_3O_4/FTO anodes, depicted as in Figure S27a, Supporting Information, played as working electrodes. Both sides of the anode—front-side coated with catalyst and the back side with only glass—were totally immersed in the electrolyte. The area test of the working electrode was 1 cm^2. The electrochemical performance of the electrodes was evaluated in a three-electrode configuration using a Pt wire as the counter electrode and a double-junction Ag|AgCl|KCl(sat.) (+0.197 V versus SHE) as the reference electrode. The scheme of the three-electrode cell setup for electrochemical measurement is illustrated in Figure S27b, Supporting Information. 1 and 0.1 M acid sulfuric (H_2SO_4) solution at pH 0.08 and 1.13, respectively, were employed as an electrolyte. The potentials were converted to the RHE scale via the Nernst equation

$$E_{RHE} = E_{Ag/AgCl} + 0.197 + 0.059 \times pH \quad (1)$$

EIS were collected at 0.3 V versus RHE and 1.8 V versus RHE over a frequency range of 0.1 Hz–200 kHz with a 5 mV amplitude. For comparison with previous publications, the overpotentials recorded in Table S5, Supporting Information, were corrected for the *iR* product, using the uncompensated resistance values for FTO from EIS in pH 0 and pH 1. ECSA

was investigated through the electrochemical capacitance current at 0.81 V versus RHE, which was measured by scanning cyclic voltammetry curves at different rates at the potential window of 0.76 to 0.86 V versus RHE. ECSA was calculated by comparing the double-layer capacitance of the Co_3O_4 anode (C_{dl}) to the specific capacitance (C_s) that ECSA = C_{dl}/C_s, where C_s is the capacitance of an atomically smooth planar surface of the material per unit area under identical electrolyte conditions, meaning identical pH and applied potential range.[59–61,78] Here, a glassy carbon surface sourced from PINE research (AFE5T050GC with a disk diameter of 5 mm) was used to measure a specific capacitance of the planar electrode. Faradaic efficiency for the OER was measured in a continuous-flow set-up, in which an air-tight H-cell was connected to a gas chromatography (GC). The high-quality argon was used as a carrier gas to pass through the electrolyte solution and then to the GC with a flow rate of 10 mL min^{-1}.

Theoretical Calculations: DFT calculations were performed using the projector augmented wave (PAW) method[79,80] as implemented in the Vienna Ab initio Simulation Package (VASP).[81,82] The calculations were completed with a plane-wave cut-off energy of 500 eV and Monkhorst–Pack k-points mesh of 3 × 3 × 1. The electronic self-consistent calculation was converged to 1×10^{-5} eV and ionic relaxation steps were performed using the conjugate-gradient method (IBRION = 2) and continued until the total force on each atom dropped below a tolerance of 3×10^{-2} eV $Å^{-1}$. The generalized gradient approximation (GGA) was used for the exchange-correlation functionals as parameterized by Perdew–Burke–Ernzerhof (PBE).[83] The adsorption energy was calculated using the following equation

$$E_{ads} = E\,(\text{slab} * \text{MO}) - E\,(\text{slab}) - E\,(\text{MO}) \quad (2)$$

where E(slab*MO), E(slab), and E(MO) are the electronic energies of Co_3O_4 surface with adsorbed oxide (MO), clean Co_3O_4 surface, and MO as adsorbate. Co_3O_4 surfaces of (011) were investigated in this study using the slab method with a vacuum thickness of 20 Å, along with different oxides of Al, Hf, Sn, Ti, and Si.

Supporting Information

Supporting Information is available from the Wiley Online Library or from the author.

Acknowledgements

A.T. acknowledges support from National Intelligence and Security Discovery Research Grants NS210100083, Australian Research Council Future Fellowship FT200100939, Australian Research Council Discovery Project DP190101864 and Australian Renewable Energy Agency - Research and Development Program, Round 4: Renewable Hydrogen for Export AS008. The authors acknowledge the financial support of the FT200100317 (Future Fellowship to ANS). The authors also acknowledge the Centre for Advanced Microscopy (CAM) and the University of New South Wales Analytical Centre for assistance in SEM, XPS, and ICP measurements. X.M.C.T. thanks Dr. Kaushal Vora and Dr. Olivier Lee Cheong Lem for supporting the sputtering and ALD deposition at the Australian National Fabrication Facility (ANFF) – ACT node.

Open access publishing facilitated by The University of Sydney, as part of the Wiley - The University of Sydney agreement via the Council of Australian University Librarians.

Conflict of Interest

The authors declare no conflict of interest.

Author Contributions

T.T.-P., X.M.C.T., and A.T. conceived the concept. X.M.C.T., T.K.A.N., L.C., and T.T.-P. synthesized the material. X.M.C.T. and T.T.-P. tested performance. X.M.C.T. and T.T.-P. cowrote a draft of the paper. X.M.C.T., A.D.B., T.T.-P., R.D., E.M., and T.N.T. carried out material characterization. J.Y. carried out the theoretical studies. T.T.-P., A.N.S., and A.T. supervised and directed the research. All authors discussed the results and contributed to the final version of the paper.

Data Availability Statement

The data that support the findings of this study are available from the corresponding author upon reasonable request.

Keywords

acidic water splitting, atomic layer deposition, Co_3O_4 anodes, HfO_2 , protection coating

Received: June 2, 2023
Revised: August 23, 2023
Published online:

[1] O. Bic Ková, P. Straka, *Int. J. Hydrogen Energy* **2012**, *37*, 11563.
[2] H. Ishaq, I. Dincer, C. Crawford, *Int. J. Hydrogen Energy* **2022**, *47*, 26238.
[3] P. J. Megía, A. J. Vizcaíno, J. A. Calles, A. Carrero, *Energy Fuels* **2021**, *35*, 16403.
[4] A. Godula-Jopek, D. Stolten, C. Bourasseau, *Hydrogen Production by Electrolysis*, WILEY-VCH Verlag GmbH & Co. KGaA, Weinheim, **2015**.
[5] S. S. Kumar, H. Lim, *Energy Rep.* **2022**, *8*, 13793.
[6] Y. Leng, G. Chen, A. J. Mendoza, T. B. Tighe, M. A. Hickner, C.-Y. Wang, *J. Am. Chem. Soc.* **2012**, *134*, 9054.
[7] K. Zeng, D. Zhang, *Prog. Energy Combust. Sci.* **2010**, *36*, 307.
[8] M. Carmo, D. L. Fritz, J. Mergel, D. Stolten, *Int. J. Hydrogen Energy* **2013**, *38*, 4901.
[9] L. Zhang, X. Jie, Z.-G. Shao, Z.-M. Zhou, G. Xiao, B. Yi, *Int. J. Hydrogen Energy* **2012**, *37*, 1321.
[10] L. Ma, S. Sui, Y. Zhai, *Int. J. Hydrogen Energy* **2009**, *34*, 678.
[11] S. S. Kumar, V. Himabindu, *Mater. Sci. Energy Technol.* **2019**, *2*, 442.
[12] J. Kibsgaard, I. B. Chorkendorff, *Nat. Energy* **2019**, *4*, 430.
[13] L. An, C. Wei, M. Lu, H. Liu, Y. Chen, G. G. Scherer, A. C. Fisher, P. Xi, Z. J. Xu, C.-H. Yan, *Adv. Mater.* **2021**, *33*, 2006328.
[14] E. Fabbri, T. J. Schmidt, *ACS Catal.* **2018**, *8*, 9765.
[15] Q. Wang, Y. Cheng, H. B. Tao, Y. Liu, X. Ma, D. Li, H. Bin Yang, B. Liu, *Angew. Chem., Int. Ed.* **2023**, *62*, e202216645.
[16] S. Cherevko, A. R. Zeradjanin, A. A. Topalov, N. Kulyk, I. Katsounaros, K. J. J. Mayrhofer, *ChemCatChem* **2014**, *6*, 2219.
[17] S. Cherevko, S. Geiger, O. Kasian, A. Mingers, K. J. J. Mayrhofer, *J. Electroanal. Chem.* **2016**, *773*, 69.
[18] S. Cherevko, S. Geiger, O. Kasian, N. Kulyk, J.-P. Grote, A. Savan, B. R. Shrestha, S. Merzlikin, B. Breitbach, A. Ludwig, K. J. J. Mayrhofer, *Catal. Today* **2016**, *262*, 170.
[19] M. A. Hubert, A. M. Patel, A. Gallo, Y. Liu, E. Valle, M. Ben-Naim, J. Sanchez, D. Sokaras, R. Sinclair, J. K. Nørskov, L. A. King, M. Bajdich, T. F. Jaramillo, *ACS Catal.* **2020**, *10*, 12182.
[20] C. C. L. Mccrory, S. Jung, I. M. Ferrer, S. M. Chatman, J. C. Peters, T. F. Jaramillo, *J. Am. Chem. Soc.* **2015**, *137*, 4347.
[21] X. Sun, K. Xu, C. Fleischer, X. Liu, M. Grandcolas, R. Strandbakke, T. Bjørheim, T. Norby, A. Chatzitakis, *Catalysts* **2018**, *8*, 657.
[22] M. Huynh, T. Ozel, C. Liu, E. C. Lau, D. G. Nocera, *Chem. Sci.* **2017**, *8*, 4779.
[23] S. Cherevko, *Curr. Opin. Electrochem.* **2023**, *38*, 101213.
[24] Z.-P. Wu, X. F. Lu, S.-Q. Zang, X. W. D. Lou, *Adv. Funct. Mater.* **2020**, *30*, 1910274.

[25] R. Frydendal, E. A. Paoli, B. P. Knudsen, B. Wickman, P. Malacrida, I. E. L. Stephens, I. B. Chorkendorff, *ChemElectroChem* **2014**, *1*, 2075.
[26] L. G. Bloor, P. I. Molina, M. D. Symes, L. Cronin, *J. Am. Chem. Soc.* **2014**, *136*, 3304.
[27] N. Li, T. P. Keane, S. S. Veroneau, R. G. Hadt, D. Hayes, L. X. Chen, D. G. Nocera, *Proc. Natl. Acad. Sci. U. S. A.* **2020**, *117*, 16187.
[28] S. Luke, M. Chatti, A. Yadav, B. V. Kerr, J. Kangsabanik, T. Williams, P. V. Cherepanov, B. Johannessen, A. Tanksale, D. R. Macfarlane, R. K. Hocking, A. Alam, A. Yella, A. N. Simonov, *J. Mater. Chem. A* **2021**, *9*, 27468.
[29] H. Du, M. Chatti, B. Kerr, C. K. Nguyen, T. Tran-Phu, D. A. Hoogeveen, P. V. Cherepanov, A. S. R. Chesman, B. Johannessen, A. Tricoli, R. K. Hocking, D. R. MacFarlane, A. N. Simonov, *ChemCatChem* **2022**, *14*, 202200013.
[30] A. E. Thorarinsdottir, C. Costentin, S. S. Veroneau, D. G. Nocera, *Chem. Mater.* **2022**, *34*, 826.
[31] D. Simondson, M. Chatti, J. L. Gardiner, B. V. Kerr, D. A. Hoogeveen, P. V. Cherepanov, I. C. Kuschnerus, T. D. Nguyen, B. Johannessen, S. L. Y. Chang, D. R. Macfarlane, R. K. Hocking, A. N. Simonov, *ACS Catal.* **2022**, *12*, 12912.
[32] C. Costentin, D. G. Nocera, *Proc. Natl. Acad. Sci. U. S. A.* **2017**, *114*, 13380.
[33] A. E. Thorarinsdottir, S. S. Veroneau, D. G. Nocera, *Nat. Commun.* **2022**, *13*, 1243.
[34] M. Chatti, J. L. Gardiner, M. Fournier, B. Johannessen, T. Williams, T. R. Gengenbach, N. Pai, C. Nguyen, D. R. Macfarlane, R. K. Hocking, A. N. Simonov, *Nat. Catal.* **2019**, *2*, 457.
[35] D. Simondson, M. Chatti, S. A. Bonke, M. F. Tesch, R. Golnak, J. Xiao, D. A. Hoogeveen, P. V. Cherepanov, J. L. Gardiner, A. Tricoli, D. R. Macfarlane, A. N. Simonov, *Angew. Chem., Int. Ed.* **2021**, *60*, 15821.
[36] J. Su, Z. Li, Y. Yu, X. Wang, *Adv. Mater. Interfaces* **2017**, *4*, 1600835.
[37] T. Wang, Z. Luo, C. Li, J. Gong, *Chem. Soc. Rev.* **2014**, *43*, 7469.
[38] A. T. Sivagurunathan, S. Adhikari, D.-H. Kim, *Nano Energy* **2021**, *83*, 105802.
[39] T. Tran-Phu, H. Chen, R. Daiyan, M. Chatti, B. Liu, R. Amal, Y. Liu, D. R. Macfarlane, A. N. Simonov, A. Tricoli, *ACS Appl. Mater. Interfaces* **2022**, *14*, 33130.
[40] Y. W. Chen, J. D. Prange, S. Dühnen, Y. Park, M. Gunji, C. E. D. Chidsey, P. C. Mcintyre, *Nat. Mater.* **2011**, *10*, 539.
[41] T. Moehl, J. Suh, L. Sévery, R. Wick-Joliat, S. D. Tilley, *ACS Appl. Mater. Interfaces* **2017**, *9*, 43614.
[42] L. Pan, J. H. Kim, M. T. Mayer, M.-K. Son, A. Ummadisingu, J. S. Lee, A. Hagfeldt, J. Luo, M. Grätzel, *Nat. Catal.* **2018**, *1*, 412.
[43] W. Kim, T. Tachikawa, D. Monllor-Satoca, H.-I. Kim, T. Majima, W. Choi, *Energy Environ. Sci.* **2013**, *6*, 3732.
[44] M. Li, Z. X. Jin, W. Zhang, Y. H. Bai, Y. Q. Cao, W. M. Li, D. Wu, A. D. Li, *Sci. Rep.* **2019**, *9*, 10438.
[45] J. S. Daubert, G. T. Hill, H. N. Gotsch, A. P. Gremaud, J. S. Ovental, P. S. Williams, C. J. Oldham, G. N. Parsons, *ACS Appl. Mater. Interfaces* **2017**, *9*, 4192.
[46] A. F. Baxter, J. Abed, D. V. Fraga Alvarez, D. Zhou, D. Kuvar, E. H. Sargent, D. Esposito, *J. Electrochem. Soc.* **2023**, *170*, 054503.
[47] Y. Liu, J. Li, W. Li, Q. Liu, Y. Yang, Y. Li, Q. Chen, *Int. J. Hydrogen Energy* **2015**, *40*, 8856.
[48] M. C. Biesinger, B. P. Payne, A. P. Grosvenor, L. W. M. Lau, A. R. Gerson, R. S. C. Smart, *Appl. Surf. Sci.* **2011**, *257*, 2717.
[49] T. Tran-Phu, R. Daiyan, J. Leverett, Z. Fusco, A. Tadich, I. Di Bernardo, A. Kiy, T. N. Truong, Q. Zhang, H. Chen, P. Kluth, R. Amal, A. Tricoli, *Chem. Eng. J.* **2022**, *429*, 132180.
[50] T. Tran-Phu, M. Chatti, J. Leverett, T. K. A. Nguyen, D. Simondson, D. A. Hoogeveen, A. Kiy, T. Duong, B. Johannessen, J. Meilak, P. Kluth, R. Amal, A. N. Simonov, R. K. Hocking, R. Daiyan, A. Tricoli, *Small* **2023**, *19*, 2208074.
[51] A. K.-V. S. W. G., C. J. P. Alexander, V. Naumkin, "NIST X-ray Photoelectron Spectroscopy Database", **n.d.**
[52] N. M. Figueiredo, N. J. M. Carvalho, A. Cavaleiro, *Appl. Surf. Sci.* **2011**, *257*, 5793.
[53] A. Dane, U. K. Demirok, A. Aydinli, S. Suzer, *J. Phys. Chem. B* **2006**, *110*, 1137.
[54] M. C. Biesinger, L. W. M. Lau, A. R. Gerson, R. S. C. Smart, *Appl. Surf. Sci.* **2010**, *257*, 887.
[55] M. C. Biesinger, B. P. Payne, B. R. Hart, A. P. Grosvenor, N. S. Mcintyre, L. W. M. Lau, R. S. Smart, *J. Phys. Conf. Ser.* **2008**, *100*, 012025.
[56] J. F. Moulder, W. F. Stickle, W. M. Sobol, K. D. Bomben, **1992**.
[57] M. Chatti, T. Gengenbach, R. King, L. Spiccia, A. N. Simonov, *Chem. Mater.* **2017**, *29*, 3092.
[58] E. Charnetskaya, M. Chatti, B. V. Kerr, T. Tran-Phu, T. D. Nguyen, P. V. Cherepanov, D. A. Hoogeveen, B. Johannessen, A. Tricoli, D. R. Macfarlane, R. K. Hocking, A. N. Simonov, *ACS Sustainable Chem. Eng.* **2022**, *10*, 7117.
[59] P. Connor, J. Schuch, B. Kaiser, W. Jaegermann, *Z. Phys. Chem.* **2020**, *234*, 979.
[60] S. Trasatti, O. A. Petrii, *J. Electroanal. Chem.* **1992**, *327*, 353.
[61] C. C. L. Mccrory, S. Jung, J. C. Peters, T. F. Jaramillo, *J. Am. Chem. Soc.* **2013**, *135*, 16977.
[62] X. M. C. Ta, T. K. A. Nguyen, A. D. Bui, H. T. Nguyen, R. Daiyan, R. Amal, T. Tran-Phu, A. Tricoli, *Adv. Mater. Technol.* **2023**, *8*, 2201760.
[63] S. Anantharaj, S. Noda, *ChemElectroChem* **2020**, *7*, 2297.
[64] M. D. Obradovic, B. D. Balanc, U. C. Lacnjevac, S. L. Gojkovic, *J. Electroanal. Chem.* **2021**, *881*, 114944.
[65] X. Deng, S. Öztürk, C. Weidenthaler, H. Tüysüz, *ACS Appl. Mater. Interfaces* **2017**, *9*, 21225.
[66] M. Favaro, J. Yang, S. Nappini, E. Magnano, F. M. Toma, E. J. Crumlin, J. Yano, I. D. Sharp, *J. Am. Chem. Soc.* **2017**, *139*, 8960.
[67] A. Bergmann, E. Martinez-Moreno, D. Teschner, P. Chernev, M. Gliech, J. F. De Araújo, T. Reier, H. Dau, P. Strasser, *Nat. Commun.* **2015**, *6*, 8625.
[68] A. G. Scheuermann, J. D. Prange, M. Gunji, C. E. D. Chidsey, P. C. Mcintyre, *Energy Environ. Sci.* **2013**, *6*, 2487.
[69] S. Wang, T. Shen, C. Yang, G. Luo, D. Wang, *ACS Catal.* **2023**, *13*, 8670.
[70] T. Reier, H. N. Nong, D. Teschner, R. Schlögl, P. Strasser, *Adv. Energy Mater.* **2017**, *7*, 1601275.
[71] A. Babaei, M. Rezaei, *J. Electroanal. Chem.* **2023**, *935*, 117319.
[72] J. Yu, F. A. Garcés-Pineda, J. González-Cobos, M. Peña-Díaz, C. Rogero, S. Giménez, M. C. Spadaro, J. Arbiol, S. Barja, J. R. Galán-Mascarós, *Nat. Commun.* **2022**, *13*, 4341.
[73] Q. Lai, V. Vediyappan, K.-F. Aguey-Zinsou, H. Matsumoto, *Adv. Energy Sustainability Res.* **2021**, *2*, 2100086.
[74] X. Yang, H. Li, A.-Y. U. Lu, S. Min, Z. Idriss, M. N. Hedhili, K.-W. Huang, H. Idriss, L.-J. Li, *Nano Energy* **2016**, *25*, 42.
[75] A. Li, S. Kong, C. Guo, H. Ooka, K. Adachi, D. Hashizume, Q. Jiang, H. Han, J. Xiao, R. Nakamura, *Nat. Catal.* **2022**, *5*, 109.
[76] I. A. Moreno-Hernandez, C. A. Macfarland, C. G. Read, K. M. Papadantonakis, B. S. Brunschwig, N. S. Lewis, *Energy Environ. Sci.* **2017**, *10*, 2103.
[77] "The Materials Project,", https://materialsproject.org/, (accessed June: 2023).
[78] T. Tran-Phu, Z. Fusco, I. Di Bernardo, J. Lipton-Duffin, C. Y. Toe, R. Daiyan, T. Gengenbach, C.-H. Lin, R. Bo, H. T. Nguyen, G. M. J. Barca, T. Wu, H. Chen, R. Amal, A. Tricoli, *Chem. Mater.* **2021**, *33*, 3553.
[79] P. E. Blöchl, *Phys. Rev. B* **1994**, *50*, 17953.
[80] G. Kresse, D. Joubert, *Phys. Rev. B* **1999**, *59*, 1758.
[81] G. Kresse, J. Furthmüller, *Phys. Rev. B* **1996**, *54*, 11169.
[82] G. Kresse, J. Furthmüller, *Comput. Mater. Sci.* **1996**, *6*, 15.
[83] J. P. Perdew, K. Burke, M. Ernzerhof, *Phys. Rev. Lett.* **1996**, *77*, 3865.